Eur. Phys. J. C (2025) 85:668
https://doi.org/10.1140/epjc/s10052-025-14405-5

THE EUROPEAN PHYSICAL JOURNAL C

Regular Article - Theoretical Physics

Some observable physical properties of Finslerian Hayward-like black hole with global monopole charge and quintessence field

Faizuddin Ahmed[1,a], **Ahmad Al-Badawi**[2,b], **İzzet Sakallı**[3,c]

[1] Department of Physics, Royal Global University, Guwahati, Assam 781035, India
[2] Department of Physics, Al-Hussein Bin Talal University, Ma'an 71111, Jordan
[3] Physics Department, Eastern Mediterranean University, North Cyprus via Mersin 10, 99628 Famagusta, Turkey

Received: 1 February 2025 / Accepted: 6 June 2025

Abstract In this work, we investigate the geodesic motion of both massless and massive test particles in the vicinity of a spherically symmetric Finslerian Hayward-like black hole (FHBH) that is coupled to a quintessence field (QF) and carries a global monopole (GM). By examining the combined effects of the GM and QF, we observe significant deviations in the geodesic structure for both null and time-like particles when compared to the conventional BH models. Additionally, we explore spin-0 scalar field perturbations by solving the massless Klein–Gordon equation in this modified BH space-time background and analyze the influence of the Finslerian geometry, GM, and QF on the resulting scalar perturbative potential. Using the effective potential derived from null geodesics, we compute the transmission and reflection coefficients and discuss their physical implications. Furthermore, we numerically calculate the quasinormal modes (QNMs) frequencies based on the scalar perturbations potential and assess how the Finslerian modifications, along with the presence of GM and QF, affect the QNM spectrum.

1 Introduction

General Relativity (GR) has been remarkably successful in describing gravitational phenomena, yet it faces significant challenges when extended to the quantum scale or to cosmological scenarios involving dark matter and dark energy [1,2]. In recent years, alternative theories of gravity have gained increasing attention as they offer insights into these unresolved issues [3,4]. Among them, Finsler geometry has emerged as a promising extension of Riemannian geometry, providing a broader mathematical framework to describe space-time structure [5,6]. Unlike GR, where the metric tensor alone defines the space-time, Finsler geometry generalizes this concept by allowing the fundamental length element to depend on both position and velocity, leading to modifications in geodesic motion and causal structure [7,8]. Such an approach is particularly useful in addressing scenarios where Lorentz symmetry breaking, anisotropic effects, or quantum gravity corrections become relevant [9–15].

Black holes (BHs) serve as an ideal setting to test the implications of modified gravity theories, as they provide a natural laboratory for studying strong gravitational effects [16,17]. One of the most extensively studied regular BH solutions is the Hayward BH (HBH), which avoids the central singularity by introducing a non-linear electrodynamics (NED) source [18–23]. The HBH solution has been widely explored in various contexts, including geodesics [24,25], thermodynamics [26,27], and QNMs [28–36]. Given the success of the HBH in addressing singularity-related issues, it is natural to investigate its modifications within the framework of Finsler geometry. A Finslerian generalization of the HBH would provide new insights into the effects of non-Riemannian space-time structures on BH physics [37,38].

The concept of Finsler space-time has been extended and refined in the literature [39–42], building upon the original framework proposed by Beem [43]. This generalized approach has been instrumental in describing a wide range of indefinite Finslerian lengths, offering a broader perspective on space-time geometry. Finslerian geometry provides a natural extension of GR, preserving the dimensionality of space-time while offering enhanced flexibility in characterizing observers, gravity, and temporal structure simultaneously [44].

Researchers have been exploring various models, including black holes, wormholes, and cosmological models,

[a] e-mail: faizuddinahmed15@gmail.com
[b] e-mail: ahmadbadawi@ahu.edu.jo
[c] e-mail: izzet.sakalli@emu.edu.tr (corresponding author)

Published online: 18 June 2025

within the framework of Finslerian geometry. These studies have spanned a wide range of theoretical investigations, contributing noticeably to our understanding of space-time dynamics and the fundamental nature of the universe. A few applications of Finslerian geometry are the Friedmann–Robertson–Walker (FRW) cosmological model [45], which describes the evolution of a homogeneous and isotropic universe. Additionally, wormhole solutions have been derived using various shape functions, including exponential ones [46,47] and other traversable wormholes [48,49] within Finslerian geometry. The Finsler–Randers (FR) metric has been explored in the context of cosmology [50], offering new insights into the role of Finslerian geometry in shaping the large-scale structure of the universe. The extension of Schwarzschild-de Sitter space-time in Finslerian geometry has also been studied [51–53]. Finslerian geometry has also been utilized in constructing models of astrophysical objects-such as charged gravastars exhibiting conformal motion [54,55] and charged anisotropic strange stars [56], contributing to our understanding of compact stellar objects in Finslerian contexts. Moreover, a few black hole solutions [57,58] and exact vacuum solution to the field equations [59] within the Finslerian geometry have been investigated. Additionally, cosmological models have studied in Finslerian background, as discussed in [60,61]. Notable studies have included the analysis of Kiselev black holes [62] and the incorporation of a quintessential field into the Hayward black hole model [63,64], providing insights into the interplay between dark energy and the geometry of black holes in a Finslerian context.

In addition to considering Finslerian modifications, we introduce a GM and a surrounding QF. A GM arises from spontaneous symmetry breaking in field theory and induces a deficit angle in spacetime, leading to significant modifications in geodesic structure and thermodynamic properties [65,66]. Meanwhile, QF serves as an effective description of dark energy, influencing the causal structure and stability of BH solutions [67,68]. The interaction among Finsler geometry, Hayward-like regularization, GM, and the QF yields intricate phenomenology necessitating detailed analysis.

The primary objective of this study is to investigate the influence of Finslerian modifications, the presence of a GM, and a surrounding QF on the geodesic motion of both massless and massive test particles in the vicinity of a FHBH. We conduct a comprehensive analysis of both null and time-like geodesics, highlighting how the combined effects of the Finslerian structure, GM, and QF introduce significant deviations in key physical features, including the effective potential, particle trajectories, and the stability of circular orbits, when compared to classical general relativistic BH models. Furthermore, we extend our investigation to scalar field perturbations by solving the massless Klein–Gordon equation in this modified background. Here, we explore how the Finslerian parameter, along with the contributions from the GM and the QF, shapes the scalar perturbative potential. Using the derived effective potential from null geodesics, we compute the transmission and reflection coefficients to analyze wave scattering behavior around the BH. In addition, we determine the QNM spectrum based on the scalar perturbation potential, with a particular focus on how Finslerian geometry, GM, and QF influence the stability characteristics of the BH.

The paper is organized as follows. In Sect. 2, we introduce the FHBH solution with GM and discuss its fundamental properties. Section 3 presents the geodesic analysis, covering effective potentials, photon sphere characteristics, and stability considerations. In Sect. 4, we examine scalar perturbations through the Klein–Gordon equation, specifically analyzing transmission and reflection probabilities. Section 5 focuses on the QNMs of the FHBH, utilizing the WKB approximation and exploring their dependence on BH parameters. Finally, in Sect. 6, we summarize our key findings and outline possible future research directions.

2 FHBH space-time with QF and GM

In this section, we introduce a metric ansatz for an FHBH surrounded by a QF that incorporates a GM. We then examine the geodesic motion, focusing on both null and time-like geodesics, and analyze in detail how the Finslerian geometry, QF, and GM influence the motion of light-like and time-like particles. Furthermore, we study the dynamics of spin-0 scalar field perturbations and discuss the behavior of the perturbative potential, highlighting the influence of the aforementioned parameters. Additionally, we calculate the QNMs spectrum and discuss the results. Therefore, the line element of a static and spherically symmetric solution describing a FHBH metric, surrounded by a QF and featuring a GM in Schwarzschild coordinates (t, r, θ, ϕ) is given by [63,64]

$$
\begin{aligned}
ds^2 &= -\mathcal{F}(r)\,dt^2 + \frac{dr^2}{\mathcal{F}(r)} + r^2\left[d\theta^2 + \sin^2(\sqrt{\gamma}\,\theta)\,d\phi^2\right],\\
\mathcal{F}(r) &= \gamma - 8\,\pi\,\eta^2 - \frac{2\,M\,r^2}{(r^3+\mathrm{g}^3)} - \frac{c}{r^{3\,w+1}},\\
\mathrm{g}^3 &= 2\,\varepsilon^2\,M.
\end{aligned}
\tag{1}
$$

Here M denotes BH mass, η being energy scale of the symmetry breaking [69,70], c is a normalization constant, w is the state parameter, and ε is the Hayward-like parameter.

This metric represents a semi-definite Finsler space, which allows us to use the covariant derivative from Riemannian geometry. Consequently, the Bianchi identities in this framework coincide with those of Riemannian geometry, specifically the covariant conservation of the Einstein tensor. The gravitational field equations can thus be derived alternatively as shown in [71]. Our paper investigates the FHBH in the

context of Finsler geometry, where Riemannian geometry is a special case. The Ricci scalar plays a significant role in shaping the FHBH structure. When $\gamma = 1$, FHBH reduces to the Riemannian case. This indicates that Finsler geometry offers a novel approach to the analysis of BH structures, distinct from the Riemannian treatment, as demonstrated in various works referenced in [72–75].

In the FHBH metric, where Ric $= \gamma =$ constant, the term $\frac{c}{r^{3w+1}}$ represents the quintessence component, and η^2 denotes the energy scale associated with spontaneous symmetry breaking. Here, M refers to the mass of the Finslerian Hayward BH, $\mathrm{g}^3 = 2\,\varepsilon^2\,M$ with ε is the Hayward-like parameter, w is the state parameter of the quintessence matter, which lies in the range $-1 < w < -1/3$, and c is a positive normalization factor used in the metric equation. When $c = 0$, the metric (1) reduces to the standard Finslerian Hayward BH. If $\mathrm{g} = 0$, the metric describes the Finslerian Schwarzschild BH, surrounded by quintessence matter [71,76]. Furthermore, when both $c = 0$ and $\mathrm{g} = 0$, the solution behaves like the Finslerian Schwarzschild BH [77], which features a single event horizon. It is important to note that a variety of BH solutions can be derived by selecting different values for the state parameter w.

The metric function $\mathcal{F}(r)$ is plotted as a function of the radial coordinate r for various values of the Finslerian parameter γ, GM parameter η, and Hayward-like parameter ε keeping fixed QF parameters ($c = 0.02$, $w = -2/3$) in Fig. 1. Moreover, a comparison of this metric function for different BHs is depicted in Fig. 2. These figures show that the space-time metric can have two horizons, one horizon, and no horizon.

The horizon structure of this FHBH space-time is governed by the parameters γ, η, ε, M, c, and w, which must satisfy specific physical bounds. For consistency with Finslerian geometry, we require $0 < \gamma < 1$; the quintessence state parameter must lie within $-1 < w < -1/3$ to ensure physically meaningful behavior; and $8\,\pi\,\eta^2 < \gamma$ to maintain positive asymptotic behavior at spatial infinity. It is worth noting that at large spatial distances, $r \gg M, \varepsilon$, the metric function approaches $\mathcal{F} \equiv \gamma - 8\,\pi\,\eta^2$ other than unity. This is occur due to the Finslerian geometry as well as the presence of GM which causes a solid angle deficit. Thus, the selected BH space-time is non-asymptotically flat.

Extremal BHs, characterized by a single degenerate horizon, occur when both $\mathcal{F}(r) = 0$ and $\mathcal{F}'(r) = 0$ at the same radius. Computing the derivative of the metric function yields:

$$\mathcal{F}'(r) = \frac{2M}{(r^3 + \mathrm{g}^3)} - \frac{6Mr\mathrm{g}^3}{(r^3 + \mathrm{g}^3)^2} + \frac{c(3w+1)}{r^{3w+2}}, \tag{2}$$

where prime denotes differentiation with respect to r. The complexity of this expression requires numerical solutions to identify extremal configurations. When the parameters do not satisfy the extremality condition, the space-time exhibits either two distinct horizons or no horizon, as shown in Figs. 1 and 2.

The horizon equation $\mathcal{F}(r) = 0$ expands to

$$\frac{2Mr^2}{r(r^3 + \mathrm{g}^3)} + \frac{c}{r^{3w+1}} = \gamma - 8\pi\eta^2, \tag{3}$$

requiring numerical methods to determine horizon radii for given parameter values.

- The parameter γ should lie within the range $0 < \gamma \leq 1$ to ensure consistency with the Finslerian framework.
- The state parameter w for the QF should be constrained within the range $-1 < w < -1/3$ to remain physically meaningful, avoiding unrealistic behaviors such as superluminal propagation or instability.
- The energy scale η should be constrained such that $8\pi\eta^2 < \gamma$ to ensure the asymptotic behavior of the metric function remains positive at spatial infinity.
- The parameters ε and c should be chosen such that they do not lead to pathological solutions, ensuring that the BH retains its regularity.

Below, we examine in detail the geodesic motion of test particles (both massless and massive) around the selected BH space-time. We analyze how the Finslerian parameter, GM, and QF influence the dynamics of test particles, and compare these effects to those observed in the standard BH scenario.

3 Geodesics motions of test particles in FHBH geometry with GM and QF

In this section, we study motions of massless photon and time-like particles in the gravitational field around the selected FHBH solution with GM and QF and analyze the outcomes. Geodesic analysis in BH physics is essential for understanding the motion of particles and light in curved space-time, showing the structure and properties of the BH. It helps determine key features-such as photon spheres, BH shadow, particle trajectories, and the stability of circular orbits, which are essential for interpreting astrophysical observations and testing gravity theories. In the present study, we employ the Lagrangian method to investigate the geodesic motion in the chosen BH background, following the approach adopted in Refs. [30–33,78–81].

The Lagrangian density function in terms of the metric tensor $g_{\mu\nu}$ can be expressed as

$$\mathcal{L} = \frac{1}{2}\, g_{\mu\nu}\, \dot{x}^{\mu}\, \dot{x}^{\nu}, \tag{4}$$

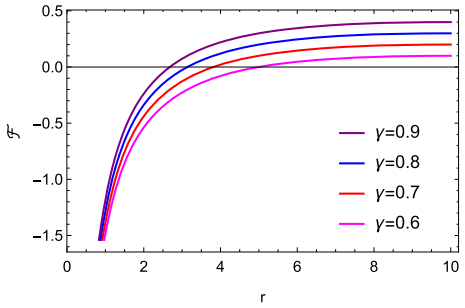

(a) $\eta^2 = 0.1, \varepsilon = 0.1$

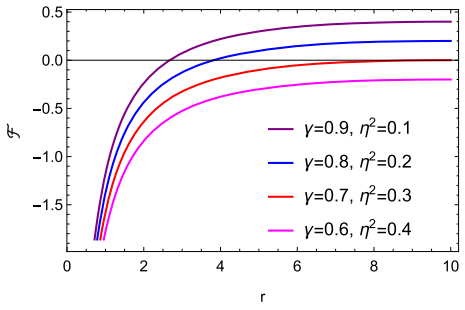

(b) $\varepsilon = 0.1$

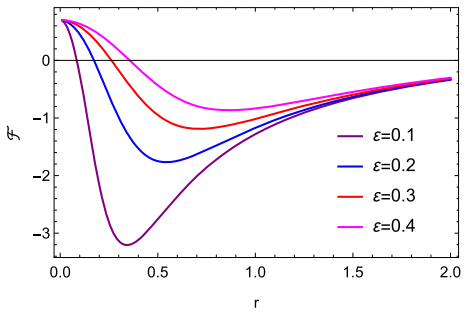

(c) $\gamma = 0.9, \eta^2 = 0.2$

Fig. 1 The behavior of the metric function $\mathcal{F}(r)$ as a function of r for various values of Finslerian parameter γ, energy scale parameter η, and Hayward-like parameter ε. Here, we set $M = 1$, $c = 0.02$, and $w = -2/3$

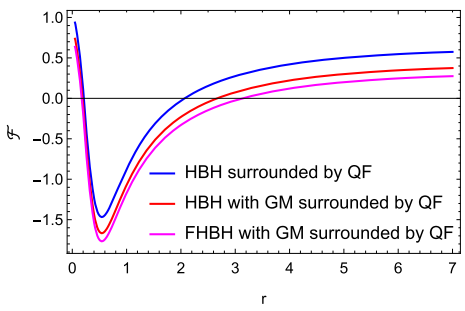

Fig. 2 A comparison of the metric function $\mathcal{F}(r)$ as a function of r for different BHs. Here, we set $M = 1, c = 0.02, w = -2/3$. Hayward BH surrounded by QF: $\gamma = 1, \varepsilon = 0.2$; Hayward BH with GM surrounded by QF: $\gamma = 1, \varepsilon = 0.2, \eta^2 = 0.2$; FHBH with GM surrounded by QF: $\gamma = 0.9, \varepsilon = 0.2, \eta^2 = 0.2$

where dot represent ordinary derivative w. r. t. an affine parameter τ.

since the selected BH space-time is static and spherically symmetric in nature, we study the geodesics motions in the equatorial plane defined by $\theta = \pi/2$. Therefore, using the metric (1), we find the Lagrangian density function (now onward calculations, $\theta = \pi/2$, so that $0 < \sin^2(\sqrt{\gamma}\,\pi/2) < 1$, where $\gamma < 1$. For simplicity, we continue with the trigonometric function)

$$\mathcal{L} = \frac{1}{2}\Big[-\mathcal{F}(r)\,\dot{t}^2 + \mathcal{F}(r)^{-1}\,\dot{r}^2 + r^2\,\sin^2(\sqrt{\gamma}\,\theta)\,\dot{\phi}^2\Big]. \quad (5)$$

From the above we see that the Lagrangian density function $\mathcal{L}$ is independent of (t, ϕ) coordinates and depends on the radial distance r. Thus, we find the following first order geodesic paths for the coordinates t, ϕ given by

$$\dot{t} = \frac{\mathrm{E}}{\mathcal{F}(r)}, \qquad \dot{\phi} = \frac{\mathrm{L}}{r^2\,\sin^2(\sqrt{\gamma}\,\theta)}, \quad (6)$$

where E, L respectively are the conserved energy and the angular momentum.

Substituting Eq. (6) into Eq. (5), we find the geodesics equation for the r coordinate as follows ($2\,\mathcal{L} = \epsilon$):

$$\dot{r} = \sqrt{\mathrm{E}^2 - V_{\mathrm{eff}}}, \quad (7)$$

where V_{eff} is the effective potential for null or time-like geodesics and it is given by

$$V_{\mathrm{eff}} = \left[-\epsilon + \frac{\mathrm{L}^2}{r^2\,\sin^2(\sqrt{\gamma}\,\theta)}\right]\Big[\gamma - 8\,\pi\,\eta^2 - \frac{2\,M\,r^2}{r^3 + \mathrm{g}^3} - \frac{c}{r^{3\,w+1}}\Big], \quad (8)$$

where $\epsilon = 0$ for null geodesics and -1 for time-like.

From the above expression of the effective potential (8), we see that various factors, such as Finslerain parameter characterize by $0 < \gamma < 1$, the energy-scale of the symmetry breaking characterize by η, the QF constant c along with state parameter w influences this effective potential both for massless and time-like test particles around the selected BH solution. This potential gets shift in comparison to the result obtained for Hayward-like BH in Riemann geometry.

3.1 Analysis of Null Geodesics: Circular null orbits, force on photon particles and photon trajectory

Null geodesics play a crucial role in analyzing various phenomena associated with the motion of photons in curved space-time. They help us understand important features such as the size of the photon sphere, the trajectories followed by photons near a BH, the angle by which light is deflected due to gravitational lensing, and the stability or instability of circular photon orbits.

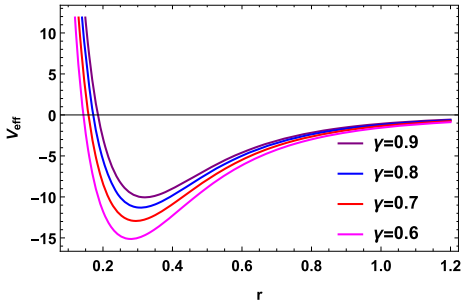

(a) $\eta^2 = 0.1$, $\varepsilon = 0.2$

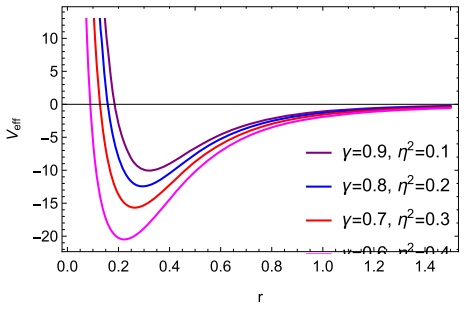

(b) $\varepsilon = 0.2$

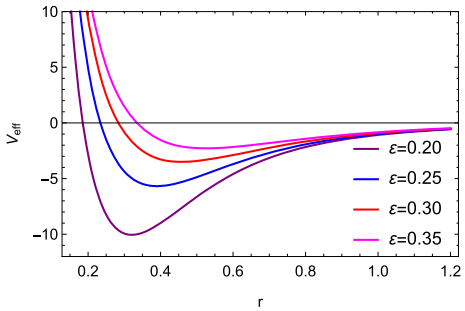

(c) $\gamma = 0.9$, $\eta^2 = 0.1$

Fig. 3 The behavior of the effective potential $V_{\rm eff}(r)$ for null geodesics as a function of r for various values of Finslerian parameter γ, the energy scale parameter η, and Hayward-like parameter ε. Here, we set $M = 1$, $c = 0.02$, and $w = -2/3$

In this part, we discuss null geodesics in detail and analyze the outcomes. For null geodesics, $\epsilon = 0$, and therefore, from Eq. (8) we find the effective potential given by

$$V_{\rm eff} = \frac{\mathrm{L}^2\left[\gamma - 8\,\pi\,\eta^2 - \frac{2\,M\,r^2}{r^3+2\,\varepsilon^2\,M} - \frac{c}{r^{3\,w+1}}\right]}{r^2\,\sin^2(\sqrt{\gamma}\,\theta)}, \tag{9}$$

In Fig. 3, we illustrate the behavior of the effective potential for null geodesics by varying different parameters of the space-time geometry, with each panel highlighting specific trends. In the top panel, we demonstrate that increasing the Finslerian parameter from $\gamma = 0.6$, while keeping the energy scale parameter $\eta^2 = 0.1$ and the Hayward-like parameter $\varepsilon = 0.2$ fixed, results in an increase of the effective potential. The middle panel shows a similar behavior: the effective potential increases as the Finslerian parameter γ is raised from 0.60 to 0.90. However, in this case, the energy scale parameter η^2 is decreased from 0.4 to 0.1, further emphasizing the interplay between these two parameters in modulating the effective potential. In the bottom panel, we observe the effective potential increasing as the Hayward-like parameter ε increases from 0.2, with the Finslerian parameter γ fixed at 0.90 and the energy scale $\eta^2 = 0.1$. Together, the Figure illustrate the inter-dependencies between the Finslerian parameter γ, the energy scale parameter η, and the Hayward-like parameter ε in shaping the effective potential for motions of photon light in the gravitational field around the selected BH space-time geometry.

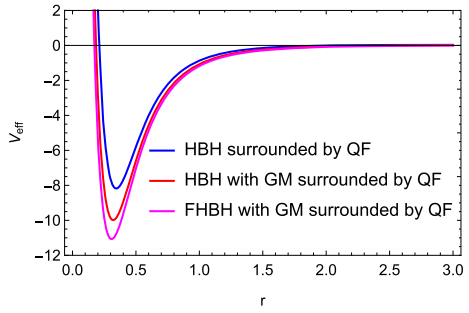

(a)

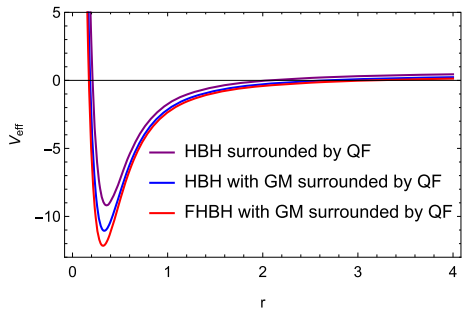

(b)

Fig. 4 A comparison of the effective potential $V_{\rm eff}(r)$ for null geodesics in **a** and time-like geodesics in **b** as a function of r for different BHs. Here, we set $M = 1$, $c = 0.02$, $w = -2/3$. Hayward BH surrounded by QF: $\gamma = 1$, $\varepsilon = 0.2$; Hayward BH with GM surrounded by QF: $\gamma = 1$, $\varepsilon = 0.2$, $\eta^2 = 0.2$; FHBH with GM surrounded by QF: $\gamma = 0.9$, $\varepsilon = 0.2$, $\eta^2 = 0.2$

In Fig. 4, we illustrate a comparison of the effective potential for both null and time-like geodesics in different BHs space-times. We observed that presence of the Finslerian parameter γ and the energy scale parameter η together decreases the effective potential for both null and time-like geodesics.

For various state parameter, w, this effective potential (9) are as follows:

(i) for $w = -1/3$,

$$V_{\rm eff} = \frac{\mathrm{L}^2\left[\gamma - 8\,\pi\,\eta^2 - \frac{2\,M\,r^2}{r^3+2\,\varepsilon^2\,M} - c\right]}{r^2\,\sin^2(\sqrt{\gamma}\,\theta)}, \tag{10}$$

(ii) for $w = -2/3$,

$$V_{\text{eff}} = \frac{\mathrm{L}^2\left[\gamma - 8\,\pi\,\eta^2 - \frac{2\,M\,r^2}{r^3+2\,\varepsilon^2\,M} - c\,r\right]}{r^2\,\sin^2(\sqrt{\gamma}\,\theta)}, \tag{11}$$

(iii) for $w = -5/6$,

$$V_{\text{eff}} = \frac{\mathrm{L}^2\left[\gamma - 8\,\pi\,\eta^2 - \frac{2\,M\,r^2}{r^3+2\,\varepsilon^2\,M} - c\,r^{3/2}\right]}{r^2\,\sin^2(\sqrt{\gamma}\,\theta)}. \tag{12}$$

To calculate the radius of an unstable photon orbit, we apply the following conditions: $V_{\text{eff}} = 0 = V'_{\text{eff}}$. Therefore, the equation for photon sphere radius is given by

$$r_{\text{ps}}\,\mathcal{F}'(r_{\text{ps}}) - 2\,\mathcal{F}(r_{\text{ps}}) = 0. \tag{13}$$

Explicitly,

$$\frac{6\,M\,r^5}{(r^3+\mathrm{g}^3)^2} + 3\,c\,r^{-1-3\,w}(1+w) - 2\,\gamma + 2\,\eta^2 = 0. \tag{14}$$

Analytically, equation (14) is extremely difficult to solve. As a result, we give numerical analysis in tables, demonstrating the effects of c and γ parameters.

Table 1 displays the numerical results r_{ps} for various γ alternatives with all BH parameters held constant. The parameter γ has a considerable impact on the radius of the photon sphere radius, with r_{ps} increasing significantly as γ values decrease. Table 2 displays the numerical results for different c selections when the BH parameters remain constant. The table shows that c has a modest impact on the photon sphere radius, with larger c values causing a slight increase in r_{ps}. Figure 5 depicts the dependency of the photon radius on the parameters γ (up) and c (down) for different values of the quintessence parameter w. Figure 5 shows that the photon radius falls significantly as the parameter γ increases. In contrast, for BH parameter c, the photon radius increases somewhat. In Fig. 5 the value of r_{ps} is consistent with the data presented in Tables 1 and 2.

Now, we study the photon trajectory in the gravitational field produced by the selected BH and analyze the result. We define the following quantity for null geodesics as,

$$\frac{\dot{r}^2}{\dot{\phi}^2} = \left(\frac{dr}{d\phi}\right)^2 = r^4\,\sin^4(\sqrt{\gamma}\,\theta)\left[\frac{1}{\beta^2} - \frac{\left(\gamma - 8\,\pi\,\eta^2 - \frac{2\,M(r)}{r} - \frac{c}{r^{3\,w+1}}\right)}{r^2\,\sin^2(\sqrt{\gamma}\,\theta)}\right], \tag{15}$$

where $\beta = \mathrm{L/E}$ is the impact parameter for photon light.

Defining a new variable $u = \frac{1}{r}$ into the Eq. (15) yields

$$\left(\frac{du}{d\phi}\right)^2 = G(u,\beta,\gamma,\eta), \tag{16}$$

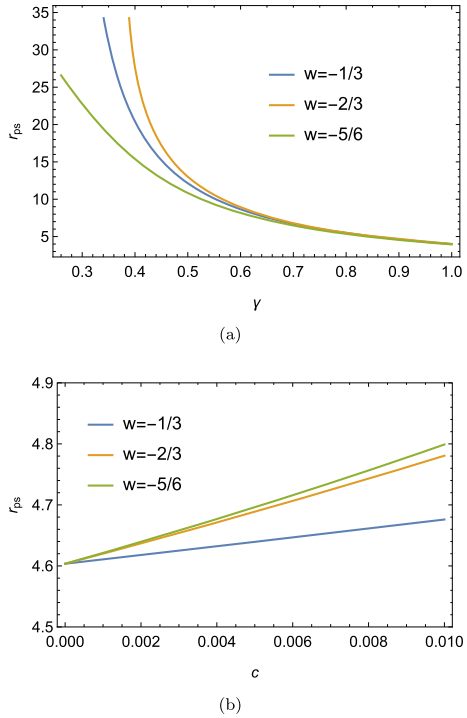

Fig. 5 Illustration of the photon sphere radius r_{ps} as a function of γ in **a** and c in **b** for various values of the state parameter w

where we defined

$$G(u,\beta,\gamma,\eta) = \frac{\sin^4(\sqrt{\gamma}\,\theta)}{\beta^2} - u^2\left(\gamma - 8\,\pi\,\eta^2 - \frac{3\,M\,u}{(1+\mathrm{g}^3\,u^3)} - c\,u^{3\,w+1}\right)\sin^2(\sqrt{\gamma}\,\theta). \tag{17}$$

Equation (16) represents the photon trajectory equation under the influence of the gravitational field produced by the chosen BH in Finslerian geometry. From this expression, it is evident that the photon trajectory is influenced by several factors, including the Finslerian parameter γ (which is constrained by $0 < \gamma < 1$), the Hayward-like parameter ε, the energy scale of symmetry breaking characterized by the parameter η, as well as the QF with constant c and the state parameter w. These factors collectively shape the path of photons in this particular space-time configuration.

Now, we compute the force acting on massless photon particles in the gravitational field produced by the chosen FHBH geometry. The force acting on the photon light can be determined in terms of the effective potential for null geodesics, as $\mathrm{F}(r) = -\frac{V'_{\text{eff}}(r)}{2}$. Using the effective potential for null geodesics provided in Eq. (9), we can express this force as:

$$\mathrm{F}(r) = \frac{\mathrm{L}^2}{r^3\,\sin^2(\sqrt{\gamma}\,\theta)}$$

Table 1 Numerical results for $r_{\rm ps}$ of the FHBH with QF under GMs for specific choices of γ. Here, $M = 1$, $\eta = 0.5$, $\mathrm{g} = (2\,\varepsilon^2\,M)^{1/3} = 0.5$, $c = 0.003$

Photon sphere radius ($r_{\rm ps}$)			
γ	$w = -1/3$	$w = -2/3$	$w = -5/6$
0.4	20.4076	27.6388	15.3688
0.6	8.64219	8.90852	8.15991
0.8	5.47612	5.52989	5.35518
1	4.00043	4.01689	3.95279

Table 2 Numerical results r_{ps} of the FHBH with quintessence under GMs for specific choices of c. Here, $M = 1$, $\eta = 0.5$, $\mathrm{g} = (2\,\varepsilon^2\,M)^{1/3} = 0.5$ and $\gamma = 0.9$

Photon sphere radius ($r_{\rm ps}$)			
c	$w = -1/3$	$w = -2/3$	$w = -5/6$
0.001	4.61073	4.62013	4.62137
0.003	4.62509	4.65394	4.65802
0.005	4.63954	4.68877	4.69617
0.007	4.65408	4.72466	4.73596

$$\times\Bigg[\gamma - 8\,\pi\,\eta^2 - \frac{3M/r}{\left(1+\frac{2\,\varepsilon^2\,M}{r^3}\right)^2} - \frac{3\,c\,(w+1)/2}{r^{3w+1}}\Bigg]. \tag{18}$$

From the above expression (18), it is clear that for different values of the state parameter w, the force acting on a massless photon varies. Furthermore, we observe that the presence of the Finslerian parameter $0 < \gamma < 1$, the energy scale of symmetry breaking characterized by the parameter η, as well as the QF with constant c and the state parameter w, all influence this force. These factors lead to a deviation from the results typically obtained in standard BH solutions within GR, causing shifts in the behavior of the force on massless photons in the gravitational field produced by the selected BH space-time in Finslerian geometry.

In Fig. 6, we illustrate the behavior of the force acting on photon particles under the influence of the gravitational field, varying different parameters of the space-time geometry. Each panel highlights specific trends. In the top panel, we show that increasing the Finslerian parameter from $\gamma = 0.6$ to less than unity, while keeping the energy scale parameter $\eta^2 = 0.1$ and the Hayward-like parameter $\varepsilon = 0.1$ fixed, results in an increase in the force. The middle panel displays a similar trend: the force increases as the Hayward-like parameter ε is raised from 0.20 to 0.35, while keeping the Finslerian parameter $\gamma = 0.9$ and the energy scale parameter $\eta^2 = 0.1$ fixed. In the bottom panel, we observe that the force decreases as the energy scale parameter increases from $\eta^2 = 0.1$ to $\eta^2 = 0.4$, while keeping the Hayward-like parameter $\varepsilon = 0.2$ and the Finslerian parameter $\gamma = 0.9$ fixed. Together, these panels illustrate the inter-dependencies between the Finslerian parameter γ, the energy scale η, and the Hayward-like parameter ε in shaping the force on massless photon light in this specific space-time geometry.

In Fig. 7, we illustrate a comparison of the force on photon particles under the influence of the gravitational field produced by different BHs space-times both in Riemann and Finslerian geometries. We observed that presence of the Finslerian parameter γ and the energy scale parameter η together decreases the force in compered to the Riemann geometry.

We present this force expression for different state parameter w as follows:

$(i)\ w = -1/3,$

$$\mathrm{F}(r) = \frac{\mathrm{L}^2}{r^3\,\sin^2(\sqrt{\gamma}\,\theta)}\left[\gamma - 8\,\pi\,\eta^2 - \frac{3M/r}{\left(1+\frac{2\,\varepsilon^2\,M}{r^3}\right)^2} - c\right], \tag{19}$$

$(ii)\ w = -2/3,$

$$\mathrm{F}(r) = \frac{\mathrm{L}^2}{r^3\,\sin^2(\sqrt{\gamma}\,\theta)}\left[\gamma - 8\,\pi\,\eta^2 - \frac{3M/r}{\left(1+\frac{2\,\varepsilon^2\,M}{r^3}\right)^2} - \frac{c\,r}{2}\right], \tag{20}$$

$(iii)\ w = -5/6,$

$$\mathrm{F}(r) = \frac{\mathrm{L}^2}{r^3\,\sin^2(\sqrt{\gamma}\,\theta)}\left[\gamma - 8\,\pi\,\eta^2 - \frac{3M/r}{\left(1+\frac{2\,\varepsilon^2\,M}{r^3}\right)^2} - \frac{c}{4}\,r^{3/2}\right]. \tag{21}$$

3.2 Analysis of time-like geodesics: circular time-like orbits, Lyapunov exponent

Time-like geodesics are the trajectories followed by massive particles, such as planets, stars etc. moving under the influ-

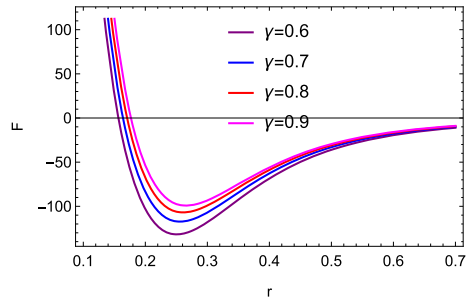

(a) $\eta^2 = 0.1$, $\varepsilon = 0.1$

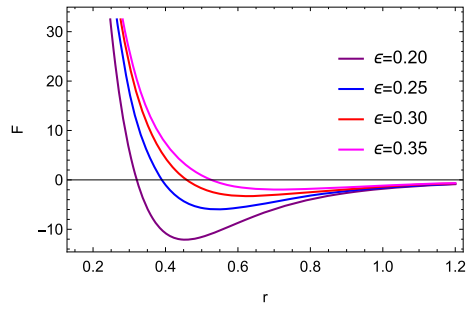

(b) $\gamma = 0.9$, $\eta^2 = 0.1$

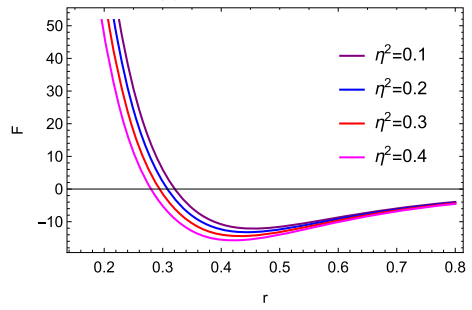

(c) $\varepsilon = 0.2$, $\gamma = 0.9$

Fig. 6 The behavior of force F(r) on massless photon particles as a function of r for various values of Finslerian parameter γ, the energy scale parameter η, and Hayward-like parameter ε. Here, we set $M = 1$, $c = 0.02$, $w = -2/3$

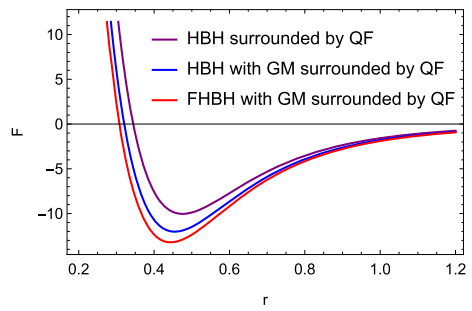

Fig. 7 A comparison of force F(r) on the massless photon particles as a function of r for different BHs. Here, we set $M = 1$, $c = 0.02$, and $w = -2/3$. Hayward BH surrounded by QF: $\gamma = 1$, $\varepsilon = 0.2$; Hayward BH with GM surrounded by QF: $\gamma = 1$, $\varepsilon = 0.2$, $\eta^2 = 0.2$; FHBH with GM surrounded by QF: $\gamma = 0.9$, $\varepsilon = 0.2$, $\eta^2 = 0.2$

ence of gravity in the curved space-time around BHs. These geodesics help determine key physical properties, including the orbital paths, velocities of particles as they revolve around the BH, and stability of circular time-like orbits. By studying time-like geodesics, we can study the dynamics of matter in accretion disks, which are critical in BH astrophysics and observational phenomena.

In this part, we study time-like geodesics in detail and analyze the results. For time-like geodesics, $\epsilon = -1$, and hence, the effective potential from Eq. (8) reduces

$$V_{\text{eff}} = \left[1 + \frac{\mathrm{L}^2}{r^2 \sin^2(\sqrt{\gamma}\,\theta)}\right]\left[\gamma - 8\,\pi\,\eta^2 - \frac{2\,M\,r^2}{r^3 + 2\,\varepsilon^2\,M} - \frac{c}{r^{3\,w+1}}\right], \tag{22}$$

For various state parameter for example, we find

$$(i)\ w = -1/3,$$
$$V_{\text{eff}} = \left[1 + \frac{\mathrm{L}^2}{r^2 \sin^2(\sqrt{\gamma}\theta)}\right]\left[\gamma - 8\pi\eta^2 - \frac{2\,M\,r^2}{(r^3 + 2\,\varepsilon^2\,M)} - c\right], \tag{23}$$
$$(ii)\ w = -2/3,$$
$$V_{\text{eff}} = \left[1 + \frac{\mathrm{L}^2}{r^2 \sin^2(\sqrt{\gamma}\theta)}\right]\left[\gamma - 8\pi\eta^2 - \frac{2\,M\,r^2}{(r^3 + 2\,\varepsilon^2\,M)} - cr\right], \tag{24}$$
$$(iii)\ w = -5/6,$$
$$V_{\text{eff}} = \left[1 + \frac{\mathrm{L}^2}{r^2 \sin^2(\sqrt{\gamma}\theta)}\right]\left[\gamma - 8\pi\eta^2 - \frac{2\,M\,r^2}{(r^3 + 2\,\varepsilon^2\,M)} - cr^{3/2}\right]. \tag{25}$$

Using the conditions of circular orbits for the time-like particles as, $\dot{r} = 0$ and $\ddot{r} = 0$, we find the following relations

$$\mathrm{E}^2 = V_{\text{eff}}, \tag{26}$$

And

$$V'_{\text{eff}}(r) = 0. \tag{27}$$

Using the effective potential (22), we find the angular momentum of time-like particles on the circular orbits in

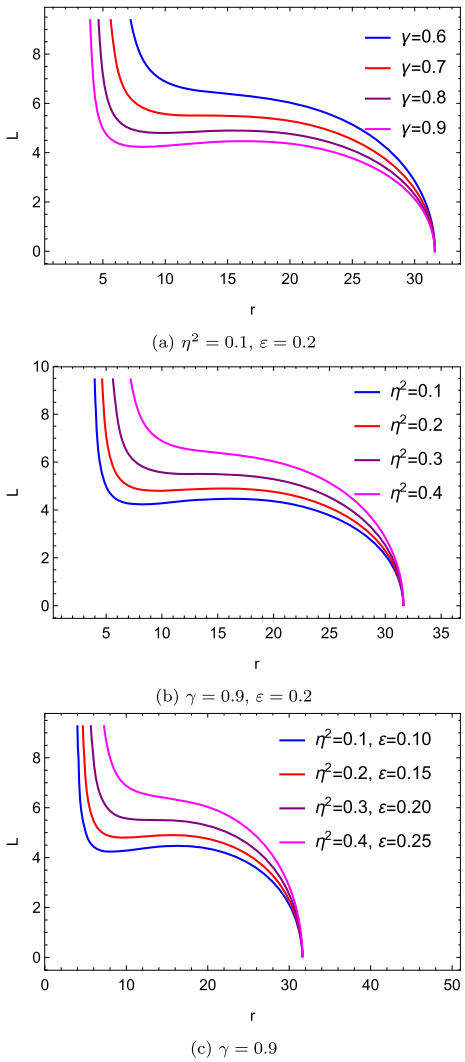

(a) $\eta^2 = 0.1$, $\varepsilon = 0.2$

(b) $\gamma = 0.9$, $\varepsilon = 0.2$

(c) $\gamma = 0.9$

Fig. 8 The behavior of particles' angular momentum $\mathrm{L}(r)$ as a function of r for various values of Finslerian parameter γ, the energy scale parameter η, and Hayward-like parameter ε. Here, we set $M = 1$, $c = 0.002$, and $w = -2/3$

the equatorial plane as,

$$\mathrm{L} = \sqrt{\frac{r^2\left[\frac{M r^2 (r^3-4\varepsilon^2 M)}{(r^3+2\varepsilon^2 M)^2} + \frac{c\,(3w+1)/2}{r^{3w+1}}\right]}{\gamma - 8\pi\eta^2 - \frac{M r^2 (3r^3+2\varepsilon^2 M)}{(r^3+2\varepsilon^2 M)^2} - \frac{3c\,(w+1)/2}{r^{3w+1}}}}. \tag{28}$$

And the time-like particles' energy on circular orbits is

$$\mathrm{E}_{\pm} = \pm \frac{\left(\gamma - 8\pi\eta^2 - \frac{2M r^2}{r^3+2\varepsilon^2 M} - \frac{c}{r^{3w+1}}\right)}{\sqrt{\gamma - 8\pi\eta^2 - \frac{M r^2 (3r^3+2\varepsilon^2 M)}{(r^3+2\varepsilon^2 M)^2} - \frac{3c\,(w+1)/2}{r^{3w+1}}}}. \tag{29}$$

From the energy expression (29), it can be seen that at spatial infinity ($r \to \infty$), the energy of the particles approaches $\mathrm{E}_{\pm} \to \pm\sqrt{\gamma - 8\pi\eta^2}$. Therefore, the maximum energy of the particles is given by $\mathrm{E}_{\pm}^{\max} = \pm\sqrt{\gamma - 8\pi\eta^2} < 1$, which depends on the Finslerian geometry parameter $0 < \gamma < 1$ and the energy scale parameter η.

From the expressions given in Eqs. (28)–(29), we observe that the time-like particle angular momentum and energy in circular orbits are influenced by several factors. These include the Finslerian parameter γ, the energy scale of symmetry breaking η, the Hayward-like parameter ε, and the QF parameters (c, w).

In Fig. 8, we illustrate the behavior of the angular momentum of time-like particles on the circular orbits in the equatorial plane under the influence of the gravitational field, varying different parameters of the space-time geometry. In the top panel, we show that increasing the Finslerian parameter from $\gamma = 0.6$ but less than unity, while keeping the energy scale parameter $\eta^2 = 0.1$ and the Hayward-like parameter $\varepsilon = 0.2$ fixed, results in a decrease in the angular momentum. In contrast, the middle panel displays the opposite trend: the angular momentum increases as the energy scale parameter η is raised from 0.1, while the Finslerian parameter $\gamma = 0.9$ and the Hyaward-like parameter $\varepsilon = 0.2$ are kept fixed. In the bottom panel, we observe a similar trend: the angular momentum of the time-like particle increases as both the energy scale parameter η and the Hayward-like parameter ε increase, while keeping the Finslerian parameter $\gamma = 0.9$ fixed. Together, these panels illustrate the interdependencies between the Finslerian parameter γ, the energy scale η^2, and the Hayward-like parameter ε in illustrating the angular momentum of time-like particles on circular orbits in this specific space-time geometry.

In Fig. 9, we illustrate the behavior of time-like particles energy on the circular orbits in the equatorial plane under the influence of the gravitational field, varying different parameters of the space-time geometry. In the top panel, we show that increasing the Finslerian parameter from $\gamma = 0.6$ but less than unity, while keeping the energy scale parameter $\eta^2 = 0.1$ and the Hayward-like parameter $\varepsilon = 0.2$ fixed, results in an increases in energy. In contrast, the middle panel displays opposite trend: the energy decreases as the energy scale parameter η is raised, while keeping the Finslerian parameter $\gamma = 0.9$ and the Hyaward-like parameter $\varepsilon = 0.2$ fixed. In the bottom panel, we observe the similar trend: energy of the time-like particle decreases as both the energy scale parameter (η) and the Hayward-like parameter (ε) increases, while keeping the Finslerian parameter $\gamma = 0.9$ fixed. Together, these panels illustrate the interdependencies between the Finslerian parameter γ, the energy scale η^2, and the Hayward-like parameter ε in illustrating the energy of time-like particles on circular orbits in this specific space-time geometry.

In Fig. 10, we present a comparison of the angular momentum (L) and energy (E) of time-like particles under the influ-

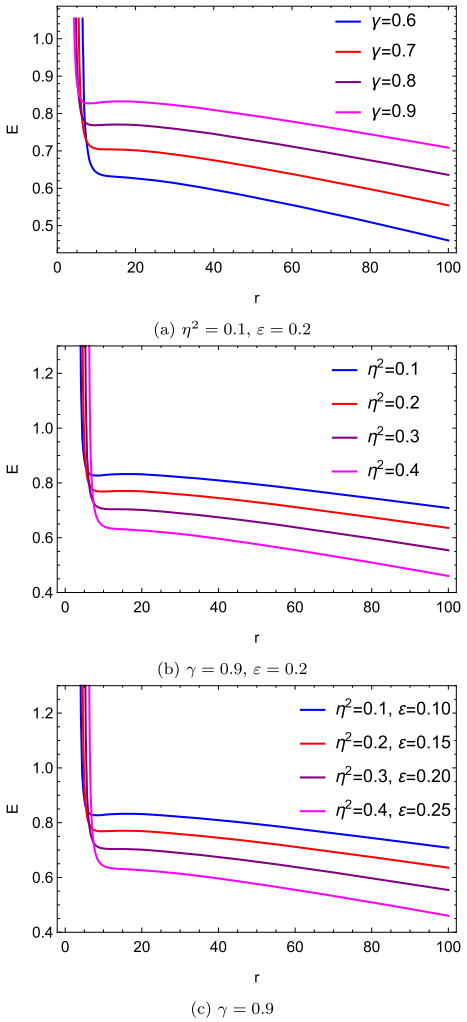

Fig. 9 The behavior of particles energy E(r) as a function of r for various values of the Finslerian parameter γ, the GM parameter η, and Hayward-like parameter ε. Here, we set $M = 1$, c=0.002, and w=-2/3

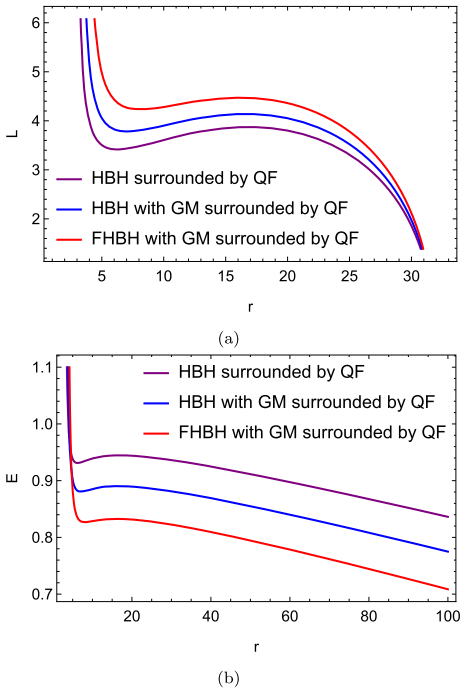

Fig. 10 A comparison of L(r) in **a** and E(r) in **b** as a function of r for different BHs. Here, we set $M = 1$, $c = 0.002$, and $w = -2/3$. Hayward BH surrounded by QF: $\gamma = 1$, $\varepsilon = 0.2$; Hayward BH with GM surrounded by QF: $\gamma = 1$, $\varepsilon = 0.2$, $\eta^2 = 0.1$; FHBH with GM surrounded by QF: $\gamma = 0.9$, $\varepsilon = 0.2$, $\eta^2 = 0.1$

ence of the gravitational field produced by BH space-times with a QF and GM, both in Riemann and Finslerian geometries. We observe that the presence of the Finslerian parameter γ and the energy scale parameter η together increase the angular momentum, whereas the energy of the particles decreases compared to the Riemann geometry, both with and without GM.

Now, we determine the angular velocity of time-like particles' on circular orbits in the equatorial plane. It is defined by [82]

$$\Omega = \sqrt{\frac{\mathcal{F}'(r)}{2\,r}} = \sqrt{\frac{M\,(r^3 - 4\,\varepsilon^2\,M)}{(r^3 + 2\,\varepsilon^2\,M)^2} + \frac{c\,(3\,w+1)/2}{r^{3\,(w+1)}}} \tag{30}$$

which is similar to the expression for Hayward-like BH with QF.

Finally, we determine the stability of the circular orbits in the equatorial plane. This stability is determine by the Lyapunov exponent as [82],

$$\lambda_L = \sqrt{\frac{2\,(\mathcal{F}'(r))^2 - \mathcal{F}(r)\,\mathcal{F}''(r) - \frac{3\,\mathcal{F}(r)\,\mathcal{F}'(r)}{r}}{2}} \tag{31}$$

Using the metric function $\mathcal{F}(r)$ given in Eq. (4), we find

$$\begin{aligned}\lambda_{\rm L} = \Bigg[& \left(\frac{2\,M\,r\,(r^3 - 4\,\varepsilon^2\,M)}{(r^3 + 2\,\varepsilon^2\,M)^2} + \frac{c\,(1+3\,w)}{r^{2+3\,w}}\right)^2 \\ & - \frac{3\left(\frac{2\,M\,r\,(r^3 - 4\,\varepsilon^2\,M)}{(r^3+2\,\varepsilon^2\,M)^2} + \frac{c\,(1+3\,w)}{r^{2+3\,w}}\right)\left(\gamma - 8\,\pi\,\eta^2 - \frac{2\,M\,r^2}{r^3+2\,\varepsilon^2\,M} - \frac{c}{r^{3\,w+1}}\right)}{2\,r} \\ & + \frac{1}{2}\left(\frac{4\,M\,\left(r^6 - 14\,r^3\,\varepsilon^2\,M + 4\,\varepsilon^4\,M^2\right)}{(r^3 + 2\,\varepsilon^2\,M)^3} + \frac{c\,(2+9\,w)\,(1+w)}{r^{3\,(1+w)}}\right) \\ & \times \left(\gamma - 8\,\pi\,\eta^2 - \frac{2\,M\,r^2}{r^3 + 2\,\varepsilon^2\,M} - \frac{c}{r^{3\,w+1}}\right)\Bigg]^{1/2}. \end{aligned} \tag{32}$$

From expression given in Eq. (32), we observe that the Lyapunov exponent for circular time-like orbits is influenced by several factors. These include the Finslerian parameter γ, the energy-scale of symmetry breaking η, the Hayward-like parameter ε, and the QF parameters (c, w).

In Fig. 11, we illustrate the behavior of the Lyapunov exponent to check the stable or unstable circular orbits in the equatorial plane under the influence of the gravitational field,

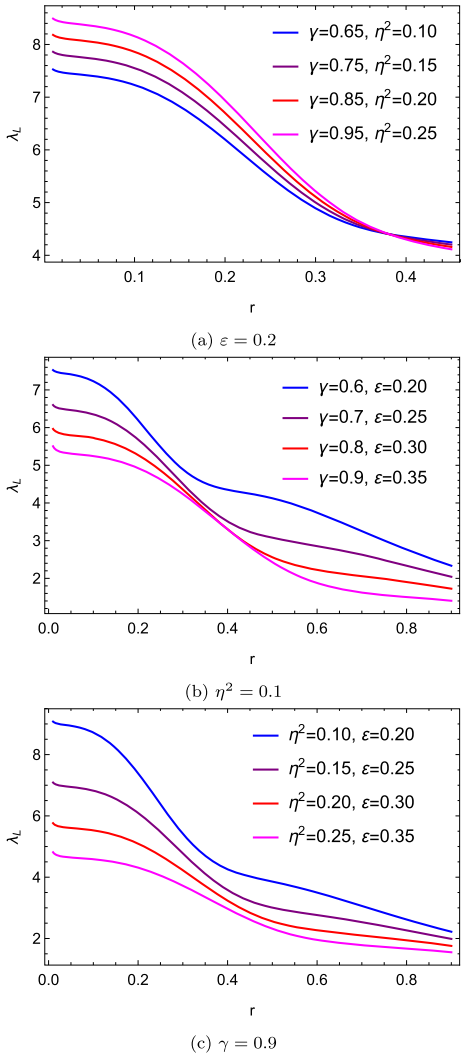

Fig. 11 The behavior of the Lyapunov exponent λ_L as a function of r for various values of Finslerian parameter γ, energy scale parameter η, and Hayward-like parameter ε. Here, we set $M = 1$, $c = 0.02$, and $w = -2/3$

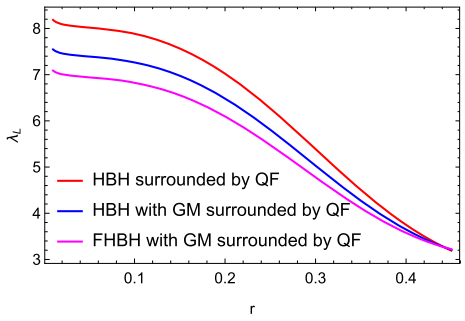

Fig. 12 A comparison of the Lyapunov exponent λ_L as a function of r for different BHs. Here, we set $M = 1$, $c = 0.02$, and $w = -2/3$. Hayward BH surrounded by QF: $\gamma = 1$, $\varepsilon = 0.2$; Hayward BH with GM surrounded by QF: $\gamma = 1$, $\varepsilon = 0.2$, $\eta^2 = 0.2$; FHBH with GM surrounded by QF: $\gamma = 0.9$, $\varepsilon = 0.25$, $\eta^2 = 0.15$

varying different parameters of the space-time geometry. In the top panel, we show that increasing the Finslerian parameter from $\gamma = 0.65$ but less than unity and the energy scale from $\eta^2 = 0.1$, while keeping the Hayward-like parameter $\varepsilon = 0.2$ fixed, results in an increases in positive value of the Lyapunov exponent. In contrast, the middle panel displays opposite trend: positive value of the Lyapunov exponent decreases as increases the Finslerian parameter γ and the Hayward-like parameter ε, while keeping the energy scale parameter $\eta^2 = 0.1$ fixed. In the bottom panel, we observe that the positive value of the Lyapunov exponent decreases as both the energy scale parameter (η) and the Hayward-like parameter (ε) increases, while keeping the Finslerian parameter $\gamma = 0.9$ fixed. Together, these panels illustrate the inter-dependencies between the Finslerian parameter γ, the energy scale η^2, and the Hayward-like parameter ε in illustrating the positive value of the Lyapunov exponent in this specific space-time geometry.

In Fig. 12, we present a comparison of the Lyapunov exponent in Riemann and Finslerian geometries. We observe that the presence of the Finslerian parameter γ and the energy scale parameter η together decreases the positive value of the Lyapunov exponent of circular time-like orbits compared to the Riemann geometry, both with and without GM. In summery, from Fig. 12, it is clear that circular time-like orbits for FHBH with GM surrounded by QF have less instability compared to Riemann geometry.

4 Scalar perturbations: the massless Klein–Gordon equation

In this section, we investigate the dynamics of a massless scalar field in the background of the selected BH solution, specifically focusing on FHBH with a GM surrounded by a QF. We begin by explicitly deriving the massless Klein–Gordon equation, which governs the evolution of the scalar field in the given space-time geometry. Our analysis emphasizes how the various parameters intrinsic to the specific BH solution, such as the Finslerain parameter, GM, and QF, influence the behavior of the scalar perturbative potential.

Scalar perturbations, in the context of BH space-times, are crucial for understanding BH stability, and the possible existence of superradiant modes. These perturbations have been widely studied in various BH solutions in GR, where they provide important insights into the nature of BH stability and the propagation of fields in curved space-time. For instance, scalar field perturbations have been analyzed in Schwarzschild, Kerr, and Reissner–Nordström BHs, along with other BHs solutions in GR and modified gravity theories (see, e.g., Refs. [30–33,83], and other related works).

To proceed for the scalar perturbations, we perform the following coordinate change (called tortoise coordinate)

$$dr_* = \frac{dr}{\mathcal{F}(r)} \tag{33}$$

into the line-element Eq. (1) along with $\theta = \tilde{\theta}/\sqrt{\gamma}$ results (finally removing tilde)

$$ds^2 = \mathcal{F}(r_*)\,\{-dt^2+dr_*^2\}+\mathcal{C}^2(r_*)\,d\theta^2+\mathcal{D}^2(r_*)\,\sin^2\theta\,d\phi^2, \tag{34}$$

where

$$\mathcal{C}^2(r_*) = r^2/\gamma, \quad \mathcal{D}^2(r_*) = r^2. \tag{35}$$

Let us consider the following wave form

$$\Phi(t, r_*, \theta, \phi) = \exp(i\,\omega\,t)\,\exp(i\,m\,\phi)\,\mathcal{Y}(\theta)\,\psi(r_*)/r_*, \tag{36}$$

where ω is (possibly complex) temporal frequency in the Fourier domain [84], m is the magnetic quantum number, $\mathcal{Y}(\theta)$ is the angular solution, and $\psi(r)$ is a propagating scalar field in the candidate space-time.

The massless scalar field wave equation is described by the Klein–Gordon equation as follows:

$$\frac{1}{\sqrt{-g}}\left[\partial_\mu(\sqrt{-g}\,g^{\mu\nu}\,\partial_\nu)\,\Phi\right] = 0, \tag{37}$$

where $g^{\mu\nu}$ is the inverse of the covariant metric tensor $g_{\mu\nu}$, g is the determinant of the covariant metric tensor, $g = \det(g_{\mu\nu})$, ∂_μ is the partial derivative, and Φ is the scalar field function.

Using the metric (34) and the wave form (36) into the wave equation (38) and after simplification, we find the Schrodinger-like equation

$$\frac{\partial^2\psi(r_*)}{\partial r_*^2} + \left(\omega^2 - \mathcal{V}\right)\,\psi(r_*) = 0, \tag{38}$$

where the scalar perturbative potential $\mathcal{V}$ is given by

$$\begin{aligned}\mathcal{V} &= \mathcal{F}\left(\frac{\lambda^2}{r^2} + \frac{\mathcal{F}'}{r}\right)\\ &= \left[\gamma - 8\,\pi\,\eta^2 - \frac{2\,M\,r^2}{r^3+2\,\varepsilon^2\,M} - \frac{c}{r^{3\,w+1}}\right]\\ &\quad\times\left[\frac{\lambda^2}{r^2} + \frac{2\,M\,(r^3-4\,\varepsilon^2\,M)}{(r^3+2\,\varepsilon^2\,M)^2} + \frac{c\,(3w+1)}{r^{3\,(w+1)}}\right].\end{aligned} \tag{39}$$

Here λ^2 is the eigenvalue of the following angular equation given by

$$\left[\frac{\gamma}{\sin\theta}\,\frac{d}{d\theta}\left(\sin\theta\,\frac{d}{d\theta}\right) - \frac{m^2}{\sin^2\theta}\right]\mathcal{Y}(\theta) = -\lambda^2\,\mathcal{Y}(\theta). \tag{40}$$

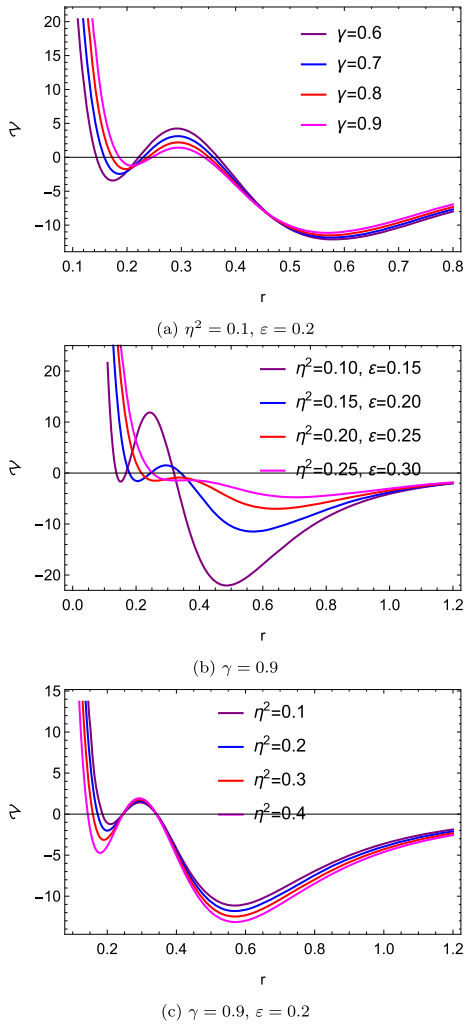

Fig. 13 The behavior of the scalar perturbative potential $\mathcal{V}$ as a function of r for various values of Finslerian parameter γ, energy scale parameter η, and Hayward-like parameter ε. Here, we set $M = 1$, $c = 0.02$, $w = -2/3$, and $k = 0$

After some straight forward calculation, we find the eigenvalue λ^2 as,

$$\lambda^2 = \left(|m| + k\,\sqrt{\gamma}\right)\left\{|m| + (k+1)\,\sqrt{\gamma}\right\} \quad (k = 0, 1, 2, ...). \tag{41}$$

Noted that for $\gamma = 1$, we will get back the well-known result $\lambda^2 = (|m| + k)\,(|m| + k + 1) = \ell\,(\ell+1)$.

From the expression given in Eq. (39), we observe that the scalar perturbative potential is influenced by several factors. These include the Finslerian parameter γ, the energy scale of symmetry breaking η, the Hayward-like parameter ε, and the QF parameters (c, w).

In Fig. 13, we illustrate the behavior of the scalar perturbative potential as we vary different parameters of the space-time geometry, including the Finslerian parameter γ,

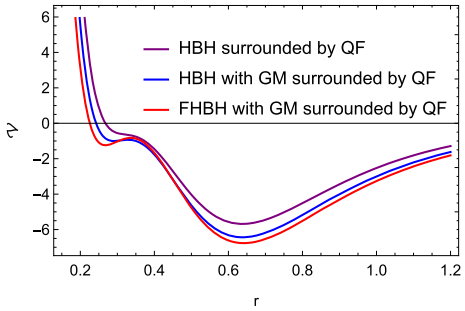

Fig. 14 A comparison of the scalar perturbative potential $\mathcal{V}$ as a function of r for different BHs. Here, we set $M = 1$, $c = 0.02$, $w = -2/3$ and $k = 0$. Hayward BH surrounded by QF: $\gamma = 1$, $\varepsilon = 0.2$; Hayward BH with GM surrounded by QF: $\gamma = 1$, $\varepsilon = 0.2$, $\eta^2 = 0.2$; FHBH with GM surrounded by QF: $\gamma = 0.9$, $\varepsilon = 0.25$, $\eta^2 = 0.15$

the energy scale η, and the Hayward-like parameter ε, for a particular state with $w = -2/3$ and $c = 0.02$ fixed. Each panel emphasizes distinct trends in the scalar potential. In Fig. 14, we provide a comparison of the scalar potential for BHs in both Riemann and Finslerian geometries.

4.1 Transmission and reflection probability

In this part we will investigate the transmission and reflection coefficients of the FHBH with GM surrounded by QF using the semi-analytic method. This method provides a general rigorous bound in the transmission and reflection probabilities for one-dimensional potential scattering [85–87]. Based on Refs. [32,85–88], the lower bound of the greybody factor is given by

$$T(\omega) \geq \sec h^2\left(\int_{-\infty}^{+\infty} \wp\, dr_*\right), \tag{42}$$

and

$$R(\omega) \leq \tan h^2\left(\int_{-\infty}^{+\infty} \wp\, dr_*\right), \tag{43}$$

where $\wp$ is defined as

$$\wp = \frac{\sqrt{(H')^2 + (\omega^2 - V_{\text{eff}} - H^2)^2}}{2H}, \tag{44}$$

where H is a positive function satisfying $H(r_*) > 0$ and $H(+\infty) = H(-\infty) = \omega$, and V_{eff} is the effective potential for null geodesics given in Eq. (9).

To obtain the transmission and reflection coefficients we will consider the scalar field potential (39) corresponds to the state parameter of the quintessence matter $w = -2/3$. Without losing generality, we can set $H^2 = \omega^2 - V_{\text{eff}}$ in Eq. (44). Therefore, the transmission and reflection coefficients become

$$T(\omega) \geq \sec h^2\left(\frac{1}{2}\int_{-\infty}^{+\infty}\left|\frac{H'}{H}\right| dr_*\right). \tag{45}$$

And

$$R(\omega) \leq \tan h^2\left(\frac{1}{2}\int_{-\infty}^{+\infty}\left|\frac{H'}{H}\right| dr_*\right). \tag{46}$$

The above integrand results $\sec h^2\left(\ln\left(\frac{H_{\text{peak}}}{H}\right)\right)$, thus to avoid divergence behaviors we split the function H into three ranges of r_*, $-\infty < r_* < r_{V_{\max}}$, $r_{V_{\max}} < r_* < r_{V_{\min}}$ and $r_{V_{\min}} < r_* < \infty$. Hence, the transmission and reflection probabilities become [88]

$$T(\omega) \geq \frac{4\,\omega^2\,(\omega^2 - V_{\text{peak}})}{\left(2\,\omega^2 - V_{\text{peak}}\right)^2}, \tag{47}$$

and

$$R(\omega) \leq \frac{V_{\text{peak}}^2}{\left(2\,\omega^2 - V_{\text{peak}}\right)^2}, \tag{48}$$

where V_{peak} is the peak of the effective potential V_{eff}.

Now we generate the Fig. 15 to investigate the influence of the Finslerian parameter γ on both the transmission and reflection probabilities. The figure shows that as γ increases, transmission probabilities decrease. Conversely, the parameter that decreases the transmission probability is expected to increase the reflection probability, as shown in the bottom panel of Fig. 15.

5 QNMs of FHBH with QF and GM

In this section, we calculate the QNMs spectrum of the scalar field discussed earlier (39), corresponding to various state parameters of the QF: $w = -1/3, -2/3$. We employ the third-order WKB approximation [89,90], using higher values of m, as the inaccuracy associated with the WKB technique decreases significantly with increasing m. Tables 3 and 4 show the dependence of the QNM frequencies on the parameters c and γ for the aforementioned state parameters, with GM parameter η fixed. We also investigate the QNMs for the index $m = 2$ and analyze the results. The behavior of the QNM frequencies demonstrates how space-time perturbations evolve in the presence of FHBH immersed in a QF and influenced by the GM.

The real component of QNMs frequency, $\text{Re}(\omega)$, determines the oscillation frequency of perturbations. For both w values, $\text{Re}(\omega)$ drops as c increases (panel (a) in Fig. 16). This normally indicates that the frequency of the perturbations'

Table 3 The QNM of the FHBH for specific choices of c

$(n = 1, \lambda = 2, M = 1, \eta = 0.5, g = 0.5, \gamma = 0.5)$		
c	$w = -1/3$	$w = -2/3$
0	$0.058224 - 0.0167487i$	$0.058224 - 0.0167487i$
0.001	$0.057879 - 0.0166196i$	$0.0539395 - 0.0151935i$
0.002	$0.057535 - 0.0164909i$	$0.0494067 - 0.0135946i$
0.003	$0.057191 - 0.0163628i$	$0.0445578 - 0.0119411i$
0.004	$0.056848 - 0.016235i$	$0.0392858 - 0.0102155i$
0.005	$0.056506 - 0.0161078i$	$0.0334049 - 0.0083867i$
0.006	$0.0561648 - 0.015981i$	$0.0265324 - 0.0063884i$
0.007	$0.0558238 - 0.015854i$	$0.0175689 - 0.0040180i$
0.008	$0.0554835 - 0.015728i$	$0.0017858 - 0.0083424i$

Table 4 The QNM of the FHBH for specific choices of γ

γ	$w = -1/3$	$w = -2/3$
0.5	$0.0565063 - 0.0161078i$	$0.0334049 - 0.0083867i$
0.6	$0.0936729 - 0.031087i$	$0.0769605 - 0.0243262i$
0.7	$0.135932 - 0.0504144i$	$0.122428 - 0.0442936i$
0.8	$0.182282 - 0.0738318i$	$0.170947 - 0.0682509i$
0.9	$0.231985 - 0.101163i$	$0.222285 - 0.0960624i$
1	$0.284501 - 0.132333i$	$0.276106 - 0.127666i$

Table 5 The QNM of the FHBH for specific choices of g

g	$w = -1/3$	$w = -2/3$
0	$0.0565014 - 0.016108i$	$0.0334016 - 0.00838674i$
0.1	$0.0565014 - 0.016108i$	$0.0334016 - 0.00838674i$
0.2	$0.0565017 - 0.016108i$	$0.0334018 - 0.00838674i$
0.3	$0.0565025 - 0.016108i$	$0.0334023 - 0.00838673i$
0.4	$0.0565039 - 0.0161079i$	$0.0334033 - 0.00838672i$
0.5	$0.0565063 - 0.0161078i$	$0.0334049 - 0.0083867i$
0.6	$0.0565099 - 0.0161077i$	$0.0334072 - 0.00838668i$
0.7	$0.056515 - 0.0161074i$	$0.0334106 - 0.00838664i$
0.8	$0.0565217 - 0.0161071i$	$0.033415 - 0.00838658i$
0.9	$0.0565303 - 0.0161068i$	$0.0334207 - 0.00838651i$
1	$0.056541 - 0.0161063i$	$0.0334278 - 0.00838642i$

oscillations decreases as the intensity of the QF surrounding it increases. The greater $\mathrm{Re}(\omega)$ for $w = -1/3$ compared to $w = -2/3$ indicates a more oscillatory character in the former condition.

$\mathrm{Im}(\omega)$, the imaginary part of the QNM frequency, determines the damping of perturbations and thus the rate of oscillation decay. $\mathrm{Im}(\omega)$ becomes less negative for both w values ($w = -1/3, -2/3$) as c increases (panel (b) in Fig. 16), implying that a higher intensity of the QF will result in a slower decay of the perturbations. This observed tendency indicates that with increasing values of c, the BH space-time becomes more "stable" in the sense that perturbations endure for a longer time.

On the other hand, for both w values ($w = -1/3, -2/3$), $\mathrm{Re}(\omega)$ increases as γ increases (panel (a) in Fig. 17). $\mathrm{Im}(\omega)$ becomes more negative as γ increases (panel (b) in Fig. 17), implying that a higher values of γ will result in a faster decay of the perturbations.

Finally, for both w values ($w = -1/3, -2/3$), $\mathrm{Re}(\omega)$ marginally increases as g grows (panel (a) in Fig. 18) while $\mathrm{Im}(\omega)$ becomes less negative as g increases (panel (b) in Fig.

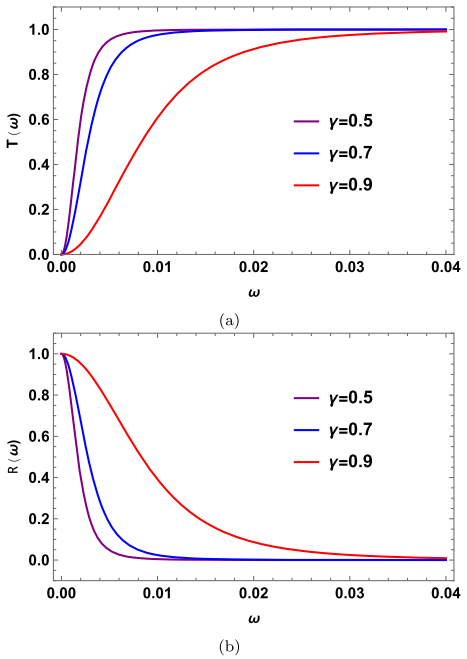

Fig. 15 Scalar field potential greybody factor in **a** and reflected factor in **b** as a function of the QNMs frequency ω for various values of the Finslerian parameter γ. The rest of the arguments are set as: $M = 1$, $\lambda^2 = 20$, $g = 0.5 = \eta$, and $c = 0.003$

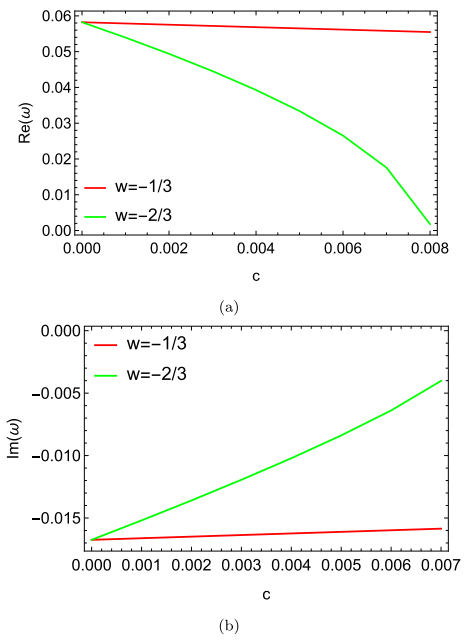

Fig. 16 The real part in **a** and imaginary part in **b** of the quasinormal frequencies for both perturbations as a function of the QF normalization constant c

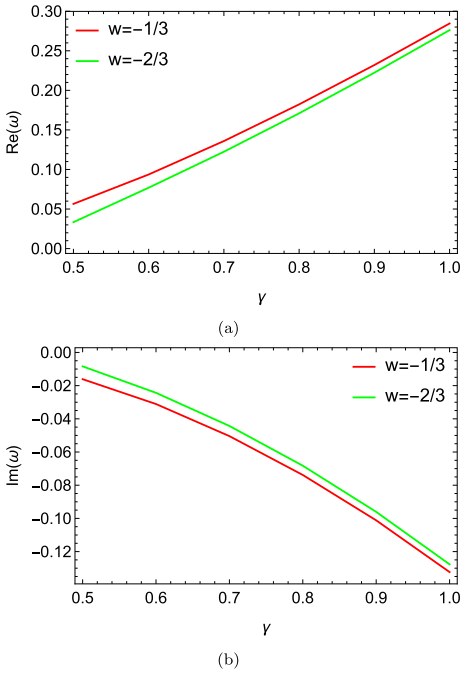

Fig. 17 The real part in **a** and imaginary part in **b** of the quasinormal frequencies for both perturbations as a function of the Finslerian parameter γ

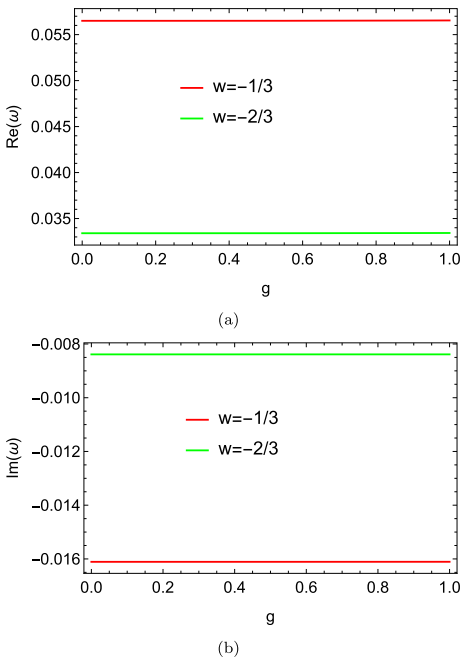

Fig. 18 The real part in **a** and imaginary part in **b** of the quasinormal frequencies for both perturbations as a function of the parameter $g = (2\,\varepsilon^2\,M)^{1/3}$

18), signaling that greater values of g will result in a slower decay of the perturbations.

6 Concluding remarks

In this study, we investigated the geodesic structure and scalar perturbations of a Finslerian Hayward-like black hole immersed in a QF, featuring a GM. Our analysis focused on understanding the influence of the Finslerian parameter γ, the QF normalization c for a specific state parameter w, the Hayward-like parameter ε, and the GM parameter η on the space-time geometry, motion of test particles, and the dynamics of scalar field perturbations.

We first introduced the space-time of a FHBH surrounded by a QF with a GM. The line element, given in Eq. (1), generalizes the known Finslerian Hayward-like metric with QF by incorporating the symmetry-breaking energy scale, or GM parameter η. The function $\mathcal{F}(r)$ was analyzed in various cases, showing distinct horizon structures depending on the values of γ, c, ε, and η. The metric structure was depicted in Figs. 1 and 2, illustrating the effect of different parameters on the existence and number of horizons.

We then explored the geodesic motion of both massless and massive test particles in this modified background. By deriving the Lagrangian density function given in Eq. (4), we obtained the conserved energy and angular momentum relations in Eq. (6). The effective potential for geodesic motion, presented in Eq. (8), demonstrated significant deviations from the conventional Hayward-like BH due to the Finslerian parameter, QF and GM. Our numerical and graphical analyses (Figs. 3, 4, 5, 6) showed how these parameters altered the motion of photon particles, affecting the location of photon sphere, dynamics of photon particles, trajectory equation etc. The radius of photon sphere $r_{\rm ps}$, which characterizes the circular trajectories of photons, was computed numerically and tabulated in Tables 1 and 2. Our results confirmed that the location of the photon sphere changes significantly with varying γ and c keeping fixed the symmetry-breaking energy scale $\eta \neq 0$. For time-like geodesics, we examined the stability of circular orbits and computed the Lyapunov exponent λ_L in Eq. (32). Figures 11 and 12 illustrated how λ_L varies with different parameters of BH, indicating that Finslerian modification enhances orbital stability compared to standard Hayward-like and Schwarzschild BHs. Additionally, the angular momentum and energy of time-like particles on circular orbits were derived in Eqs. (28) and (29), respectively, and their behavior was depicted in Figs. 8 and 9.

To analyze wave dynamics in the background of FHBH, we studied the massless scalar field governed by the Klein–Gordon equation (37). Using the tortoise coordinate transformation (33), we obtained the Schrödinger-like wave equation (38) with the effective potential $\mathcal{V}(r)$ given in Eq. (39). The behavior of the scalar potential was examined in Figs. 13 and 14, showing its dependence on γ, η, and ε. The eigenvalue equation for the angular part of the wave function was solved, leading to the expression for λ^2 in Eq. (41). Furthermore, we computed the transmission and reflection probabilities using the WKB approximation, deriving lower bounds for the greybody factors in Eqs. (47) and (48) by employing the effective potential $V_{\rm eff}$ for null geodesics given in Eq. (9). Figure 15 illustrated how the Finslerian parameter affects the transmission and reflection coefficients, demonstrating that larger values of γ increase the reflectivity of the BH. We also computed QNM frequencies using the third-order WKB method [89]. Our numerical results, summarized in Tables 3, 4, and 5, showed that increasing the QF parameter c reduced the real part of the QNM frequency while also decreasing the damping rate. The Finslerian modification was found to significantly alter the QNM spectrum, suggesting potential observational signatures.

In summary, our findings highlighted the impact of Finslerian modifications on geodesic motion, stability of circular orbits, and wave dynamics in the presence of a GM and a QF. The results provide insights into the rich phenomenology of modified gravity theories incorporating non-Riemannian geometries. For future research, it would be valuable to extend this study to include rotating FHBHs to investigate the interplay between Finslerian modifications and frame-dragging effects. Additionally, an exploration of the shadow cast by such BHs in the presence of an accretion disk could provide further observational constraints on the Finslerian parameters. Another promising direction is the study of energy extraction mechanisms such as the Penrose process and superradiance in this modified space-time [91–94]. Ultimately, exploring higher-dimensional extensions and embedding the Finslerian BH solution within string-theory-inspired gravity models may yield a profound theoretical understanding.

Acknowledgements We express our gratitude to the anonymous reviewers and the editor for their insightful feedback and support. F.A. acknowledges the Inter University Centre for Astronomy and Astrophysics (IUCAA), Pune, India for granting visiting associateship. İ. S. thanks TÜBİTAK, ANKOS, and SCOAP3 for funding and acknowledges the networking support of COST Actions CA22113, CA21106, and CA23130.

Data Availability Statement No data were generated or analyzed in this study. [Author's comment: This is a theoretical work and no new data were generated and/or analyzed in the current study].

Declarations

Code availability No code/software associated with this manuscript. [Author's comment: No code/software were generated in the current study].

Funded by SCOAP[3].

References

1. A. Einstein, Sitzungsber. Preuss. Akad. Wiss. Berlin (Math. Phys.) **1915**, 844 (1915)
2. C.M. Will, Living Rev. Relativ. **17**, 4 (2014)
3. T. Clifton, P.G. Ferreira, A. Padilla, C. Skordis, Phys. Rep. **513**, 1 (2012)
4. S. Capozziello, M. De Laurentis, Phys. Rep. **509**, 167 (2011)
5. H. Rund, *The Differential Geometry of Finsler Spaces* (Springer, New York, 1959)
6. D. Bao, S.S. Chern, Z. Shen, *An Introduction to Riemann–Finsler Geometry* (Springer, New York, 2000)
7. S. Sonego, M. Pin, J. Math. Phys. **50**, 042902 (2009)
8. I.P. Lobo, N. Loret, F. Nettel, Phys. Rev. D **95**, 046015 (2017)
9. V.A. Kostelecky, Phys. Rev. D **69**, 105009 (2004)
10. V. Perlick, Gen. Relativ. Gravit. **38**, 365 (2006)
11. M. Schreck, Phys. Rev. D **92**, 125032 (2015)
12. D. Mattingly, Living Rev. Relativ. **8**, 5 (2005)
13. İ Sakallı, S. Kanzi, Turk. J. Phys. **46**, 51 (2022)
14. R. Bluhm, Chapter: overview of the standard model extension: implications and phenomenology of Lorentz violation, in *Special Relativity. Lect. Notes Phys.*, vol. 702, ed. by J. Ehlers et al. (Springer, Berlin, 2006), pp.191–226
15. T. Tangphati, I. Sakalli, A. Banerjee, A. Pradhan, Chin. Phys. C **49**, 025110 (2025)
16. E. Berti, E. Barausse, V. Cardoso et al., Class. Quantum Gravity **32**, 243001 (2015)
17. V. Cardoso, L. Gualtieri, Class. Quantum Gravity **33**, 174001 (2016)
18. S.A. Hayward, Phys. Rev. Lett. **96**, 031103 (2006)
19. M. Amir, S.G. Ghosh, JHEP **07**, 015 (2015)
20. S.H. Mehdipour, M.H. Ahmadi, Nucl. Phys. B **926**, 49 (2018)
21. A. Kumar, D.V. Singh, S.G. Ghosh, Ann. Phys. NY **419**, 168214 (2020)
22. S.I. Kruglov, Ann. Phys. **529**, 1700073 (2017)
23. İ Sakalli, E. Guendelman, D. Singleton, S. Habib Mazharimousavi, Adv. High Energy Phys. **2018**, 5874973 (2018)
24. A. Abdujabbarov, M. Amir, B. Ahmedov, S.G. Ghosh, Phys. Rev. D **93**, 104004 (2016)
25. A. Abdujabbarov, B. Ahmedov, N. Dadhich, F. Atamurotov, Phys. Rev. D **96**, 084017 (2017)
26. J.M. Bardeen, B. Carter, S.W. Hawking, Commun. Math. Phys. **31**, 161 (1973)
27. S.W. Hawking, Commun. Math. Phys. **43**, 199 (1975) (Erratum: Commun. Math. Phys. 46, 206 (1976))
28. R.A. Konoplya, A. Zhidenko, Rev. Mod. Phys. **83**, 793 (2011)
29. E. Chaverra, J.C. Degollado, C. Moreno, O. Sarbach, Phys. Rev. D **93**, 123013 (2016)
30. A. Al-Badawi, F. Ahmed, Chin. J. Phys. **94**, 185 (2025)
31. F. Ahmed, A. Al-Badawi, İ Sakallı, A. Bouzenada, Nucl. Phys. B **1011**, 116806 (2025)
32. F. Ahmed, A. Al-Badawi, İ Sakallı, S. Kanzi, Phys. Dark Universe **48**, 101907 (2025)
33. F. Ahmed, J. Goswami, A. Bouzenada, Eur. Phys. J. C **85**, 110 (2025)
34. A. Uniyal, S. Kanzi, İ Sakallı, Eur. Phys. J. C **83**, 668 (2023)
35. A. Al-Badawi, S. Kanzi, İ Sakallı, Ann. Phys. (NY) **452**, 169294 (2023)
36. A. Al-Badawi, S. Shaymatov, Commun. Theor. Phys. **77**, 035402 (2025)
37. Z. Chang, X. Li, Phys. Lett. B **668**, 453 (2008)
38. C. Lammerzahl, V. Perlick, W. Hasse, Phys. Rev. D **86**, 104042 (2012)
39. C. Pfeifer, M.N.R. Wohlfarth, Phys. Rev. D **85**, 064009 (2012)
40. C. Lammerzahl, V. Perlick, W. Hasse, Phys. Rev. D **86**, 104042 (2012)
41. M.A. Javaloyes, M. Sánchez, Fís. Nat. Ser. A. Mat. **114**, 30 (2019)
42. M. Hohmann, C. Pfeifer, N. Voicu, Phys. Rev. D **100**, 064035 (2019)
43. J.K. Beem, Can. J. Math. **22**, 1035 (1970)
44. C. Pfeifer, *The Finsler spacetime framework: back grounds for physics beyond metric geometry*, Ph.D. Thesis (Hamburg University, 2013)
45. A.P. Kouretsis, M. Stathakopoulos, P.C. Stavrinos, Phys. Rev. D **79**, 104011 (2009)
46. F. Rahaman, N. Paul, A. Banerjee, S.S. De, S. Ray, A.A. Usmani, Eur. Phys. J. C **76**, 246 (2016)
47. H.M. Manjunatha, S.K. Narasimhamurthy, Chin. J. Phys. **77**, 1561 (2022)
48. T. Sanjay, S.K. Narasimhamurthy, Z. Nekouee, H.M. Manjunath, Pramana J. Phys. **98**, 16 (2024)
49. B.R. Yashwanth, S.K. Narasimhamurthy, Z. Nekouee, Particles **7**(3), 747 (2024)
50. Z. Nekouee, S.K. Narasimhamurthy, H.M. Manjunatha, S.K. Srivastava, Eur. Phys. J. Plus **137**, 1388 (2022)
51. H.M. Manjunatha, S.K. Narasimhamurthy, S.K. Srivastava, Pramana J. Phys. **97**, 90 (2023)
52. X. Li, X. Zhang, H.N. Lin, Phys. Rev. D **106**, 064043 (2022)
53. J.T. Yao, X. Li, Phys. Rev. D **108**, 084067 (2023)
54. T. Sanjay, S.K. Narasimhamurthy, Z. Nekouee, H.M. Manjunath, Eur. Phys. J. C **84**, 393 (2024)
55. S. Banerjee, S. Ghosh, N. Paul, F. Rahaman, Eur. Phys. J. Plus **135**, 185 (2020)
56. S.R. Chowdhury, D. Deb, F. Rahaman, S. Ray, Eur. Phys. J. C **79**, 547 (2019)
57. Z. Nekouee, S.K. Narasimhamurthy, B.R. Yashwanth, T. Sanjay, Class. Quantum Gravity **42**, 045002 (2025)
58. S.I. Vacaru, Class. Quantum Gravity **27**, 105003 (2010)
59. X. Li, Z. Chang, Phys. Rev. D **90**, 064049 (2014)
60. Z. Nekouee, H. Chaudhary, S.K. Narasimhamurthy, S.K.J. Pacif, M. Malligawad, J. High Energy Astrophys. **44**, 19 (2024)
61. Z. Nekouee, S.K. Narasimhamurthy, B. Pourhassan, S.K.J. Pacif, Ann. Phys. (NY) **470**, 169787 (2024)
62. Z. Nekouee, S.K. Narasimhamurthy, Eur. Phys. J. C **83**, 723 (2023)
63. B.R. Yashwanth, S.K. Narasimhamurthy, Z. Nekouee, M. Malligawad, Eur. Phys. J. C **84**, 1276 (2024)
64. M. Malligawad, S.K. Narasimhamurthy, Z. Nekouee, Phys. Lett. B **856**, 138963 (2024)
65. M. Barriola, A. Vilenkin, Phys. Rev. Lett. **63**, 341 (1989)
66. E.R. Bezerra de Mello, A.A. Saharian, Class. Quantum Gravity **29**, 135007 (2012)
67. V.V. Kiselev, Class. Quantum Gravity **20**, 1187 (2003)
68. S. Chen, B. Wang, R. Su, Phys. Rev. D **77**, 124011 (2008)
69. M. Barriola, A. Vilenkin, Phys. Rev. Lett. **63**, 341 (1989)
70. E.R. Bezerra de Mello, Braz. J. Phys. **31**, 211 (2001)
71. X. Li, S. Wang, Z. Chang, Commun. Theor. Phys. **61**, 781 (2014)

72. N. Ksh, F. Singh, D. Rahaman, S.K. Deb, Front. Phys. **10**, 1038905 (2023)
73. H.M. Manjunatha, S.K. Narasimhamurthy, Chin. J. Phys. **77**, 1561 (2022)
74. M. Malligawad, S.K. Narasimhamurthy, Z. Nekouee, M.Y. Kumbar, Phys. Scr. **99**, 045206 (2024)
75. T. Sanjay, S.K. Narasimhamurthy, Z. Nekouee, H.M. Manjunatha, Pramana J. Phys. **98**, 16 (2024)
76. V.V. Kiselev, Class. Quantum Gravity **20**, 1187 (2003)
77. J.T. Yao, X. Li, Phys. Rev. D **108**, 084067 (2023)
78. F. Ahmed, EPL **142**, 39002 (2023)
79. F. Ahmed, Int. J. Geom. Methods Mod. Phys. **21**, 2450187 (2024)
80. B. Hamil, B.C. Lutfuoglu, F. Ahmed, Z. Yousaf, Nucl. Phys. B **1014**, 116861 (2025)
81. F. Ahmed, İ Sakallı, A. Al-Badawi, Phys. Lett. B **464**, 139448 (2025)
82. V. Cardoso, A.S. Miranda, E. Berti, H. Witek, V.T. Zanchin, Phys. Rev. D **79**, 064016 (2009)
83. S. Fernando, Gen. Relativ. Gravit. **44**, 1857 (2012)
84. T. Regge, J.A. Wheeler, Phys. Rev. **108**, 1063 (1957)
85. M. Visser, Phys. Rev. A **59**, 427 (1999)
86. P. Boonserm, M. Visser, Ann. Phys. (NY) **323**, 2779 (2008)
87. P. Boonserm, Ph.D. Thesis (Victoria University of Wellington, 2009). arXiv:0907.0045 [math-ph]
88. P. Boonserm, S. Phalungsongsathit, K. Sansuk, P. Wongjun, Eur. Phys. J. C **83**, 657 (2023)
89. S. Iyer, C.M. Will, Phys. Rev. D **35**, 3621 (1987)
90. P. Boonserm, M. Visser, Phys. Rev. D **78**, 101502 (2008)
91. R. Penrose, R.M. Floyd, Nature **229**, 177 (1971)
92. J.M. Bardeen, W.H. Press, S.A. Teukolsky, Astrophys. J. **178**, 347 (1972)
93. S.A. Teukolsky, W.H. Press, Astrophys. J. **193**, 443 (1974)
94. R. Brito, V. Cardoso, P. Pani, *Superradiance: New Frontiers in Black Hole Physics (Lect. Notes Phys.)*, vol. 906 (Springer, Cham, 2020)